Thinning and surface mass balance patterns of two neighboring debris-covered glaciers in southeastern Tibetan Plateau

Chuanxi Zhao[1,2], Wei Yang[2*], Evan Miles[3], Matthew Westoby[4], Marin Kneib[3,5], Yongjie Wang[2], Zhen
5   He[2,6] and Francesca Pellicciotti[3,4]

[1] College of Earth and Environmental Sciences, Lanzhou University, Lanzhou, 730000, China
[2] State Key Laboratory of Tibetan Plateau Earth System, Environment and Resources (TPESER), Institute of Tibetan Plateau
Research, Chinese Academy of Sciences, Beijing, 100101, China
[3] High Mountain Glaciers and Hydrology Group, Swiss Federal Institute, WSL, Birmensdorf, 8903, Switzerland.
10 [4] Department of Geography and Environmental Sciences, Northumbria University, Newcastle upon Tyne, NE1 8ST, UK
[5] Institute of Environmental Engineering, ETH Zurich, Zurich, 8093, Switzerland
[6] University of Chinese Academy of Sciences, Beijing, 100049, China

Correspondence to: Wei Yang (yangww@itpcas.ac.cn)

Abstract. Debris-covered glaciers are a common feature of the mountain cryosphere in the southeastern Tibetan Plateau. A
15 better understanding of these glaciers change is necessary to reduce the uncertainties of the regional water resource
variability, and to anticipate potential cryospheric risks. In this study, we quantify seasonal thinning (dh) and surface mass
balance (SMB) patterns of two neighboring debris-covered glaciers (23K Glacier and 24K Glacier) in the southeastern
Tibetan Plateau with repeated unpiloted aerial vehicle (UAV) surveys and *in-situ* measurements. We observe that the dh
pattern of 23K Glacier is distinct from that of 24K Glacier, despite their proximity. The dh magnitude of the 23K Glacier is
20 ~1.4-3.0 times greater than that of the 24K Glacier at all periods, which is mainly driven by the stronger dynamic state of
24K Glacier. The contrasted behaviour between the two glaciers is also valid in the early twenty-first century. In contrast, the
SMB patterns of the two glaciers are generally in agreement at different periods. The debris thickness distribution correlates
with the SMB spatial distribution for both glaciers, while the supraglacial ice cliffs and ponds area density distribution is not
correlated with SMB spatial distribution. This high-resolution comparison study of two neighboring glaciers confirms the
25 significance of both glacier dynamic and debris thickness in controlling the thinning and melt for the different type debris-
covered glaciers of the southeastern Tibetan Plateau in the context of climate change.

1 Introduction

Monsoon-influenced glaciers in the southeastern Tibetan Plateau have experienced more significant mass loss than in most
other regions of High Mountain Asia in the past two decades (Kääb et al., 2012; Yao et al., 2012; Brun et al., 2017; Shean et
30 al., 2020; Hugonnet et al., 2021). The percentage of debris-covered area as a proportion of the total glacierised area in the
southeastern Tibetan Plateau was estimated at ~17-19%, which exceeds the proportion of debris-covered glaciers at the
global scale (~4.4%-7.3%; Scherler et al., 2018; Herreid and Pellicciotti, 2020). Notably, the rate of thinning of debris-
covered glaciers is close to that of debris-free glaciers in the southeastern Tibetan Plateau (Neckel et al., 2017; Brun et al,

2019; Ke et al., 2020), therefore a deeper understanding the evolution and mass balance patterns of debris-covered glaciers
35   in the southeastern Tibetan Plateau is essential for understanding changes in regional water resources (Zhang et al., 2011;
Neckel et al., 2017) and the mechanism of potential glacier-related hazards such as the glacial lake outburst floods (Wang et
al., 2011; Allen et al., 2019) or ice-rock avalanches in the southeastern Tibetan Plateau (Kääb et al., 2021; An et al., 2022;
Zhao et al., 2022).

Debris-covered glaciers are globally widespread (Scherler et al., 2018; Herreid and Pelicciotti, 2020), and their response to
40   climate change is considerably different to that of debris-free glaciers due to the melt-buffering effect of supraglacial debris
cover that exceed a few centimeters in thickness (Østrem, 1959; Nakawo et al., 1999; Nicholson and Benn, 2006; Reid and
Brock, 2010; Yang et al., 2017). Despite this difference, some studies have found that the debris-covered glaciers and debris-
free glaciers possess comparable thinning rates (Kääb et al., 2012; Immerzeel et al., 2013; Gardelle et al., 2013; Pelicciotti
et al., 2015; Brun et al., 2019), and this phenomenon has been called the "debris-covered anomaly" (Pelicciotti et al., 2015;
45   Vincent et al., 2016). This anomaly could partly be explained by the presence of ice cliffs and ponds at the surface of these
glaciers. Ice cliffs and supraglacial ponds are common features of debris-covered glaciers (Sakai et al., 1998, 2000), they are
directly exposed to incoming radiations and therefore act as melt 'hotspots' (Sakai, 1998, 2002; Reid and Brock, 2014; Juen
et al., 2014; Steiner et al., 2015; Buri et al., 2016; Miles et al., 2016; Miles et al., 2018; Buri et al., 2021). The areas
influenced by cliffs and ponds are characterized by high thinning and melt rates (~ 6–10 times) relative to surrounding
50   debris-covered ice in the southeastern Tibetan Plateau (Miles et al., 2022), as revealed by the differencing of high-resolution
DEMs and the results of energy-balance modelling (Thompson et al., 2016; Brun et al., 2018; Miles et al., 2018, 2022; Buri
et al., 2016, 2021; Kneib et al., 2022; Sato et al., 2021; Mishra et al., 2021). There is a debate on the so-called 'debris cover
anomaly' phenomenon since some research considers that the insulating effect of debris cover has a larger effect on total
thinning than the enhanced ice ablation due to exposed ice cliffs and supraglacial ponds (e.g., Hambrey et al., 2008; Vincent
55   et al., 2016; Brun et al, 2018; Anderson et al, 2021a). Some studies have confirmed the effect of the debris thickness spatial
distribution on the physical mechanisms of ablation (Mihalcea et al., 2008; Zhang et al., 2011; Reid et al., 2012; Juen et al.,
2014; Gibson et al., 2017; McCarthy et al., 2017). One also needs to take into account the contribution of glacier dynamics
on glacier thinning, which could be reduced for long, stagnating debris-covered glacier tongues (Nuimura et al., 2017; Brun
et al., 2018; Anderson et al., 2021a, 2021b; Rounce et al., 2021). This has led to the hypothesis that the similar thinning rates
60   of debris-covered and debris-free glaciers in High Mountain Asia is primarily caused by differences in ice dynamics
(Nuimura et al., 2017; Brun et al., 2018; Rounce et al., 2021).

Since ice cliffs and supraglacial ponds tend to have a relatively small area and be very dynamic (Miles et al., 2017; Kneib et
al., 2021), it is challenging to accurately track their evolution over time and quantify their contribution to melt (Mishra et al.,
2021; Kneib et al., 2022). Because of these challenges, studies which have investigated their spatial distribution, dynamics,
65   and melt contribution have typically utilized unpiloted aerial vehicle (UAV) or very high-resolution optical satellite data

The Cryosphere
Discussions

(Immerzeel et al., 2014; Brun et al., 2016; Brun et al., 2018; Mölg et al., 2019; Anderson et al., 2021a; Kneib et al., 2021, 2022; Mishra et al., 2021; Sato et al., 2021). These studies confirm the potential for investigating glacier- or sub-glacier-scale domains based on high-resolution data, which can provide detailed observations of local processes (e.g., Westoby et al., 2020). In the meantime，high-resolution data are also required for disentangling the glaciers thinning patterns. The use of UAVs can overcome some shortcomings associated with in-situ (i.e. ground-based) observation (e.g., limited spatial representation) and satellite remote sensing data (e.g. insufficient resolution and vulnerability to cloudy and rainy weather) hence the increasing application of UAV technology in glaciological studies worldwide, including in debris-covered glacier settings (Hugenholtz et al., 2013; Immerzeel et al., 2014; Kraaijenbrink et al., 2016; Wigmore and Mark, 2017; Fugazza et al., 2018; Rossini et al., 2018; Bash and Moorman, 2020; Westoby et al., 2020; Cao et al., 2021; Mishra et al., 2021; Xu et al., 2022). High-precision digital elevation models (DEMs) and orthophotos can be obtained relatively easily from UAV images processed using Structure-from-Motion (UAV-SfM) with multi-view stereo photogrammetry (Westoby et al., 2012; Benoit et al., 2019).

Here we systematically compare the glacier change patterns of two neighboring debris-covered glaciers, 23K Glacier and 24K Glacier, in the southeastern Tibetan Plateau for the period from 13th August 2019 to 22nd October 2020 by using change detection applied to high-resolution repeated DEMs acquired via UAV-SfM surveys, and *in-situ* measurements. The glaciers are located in the same catchment climatic setting, but the topography of the glaciers, as well as their dynamic behaviors and supraglacial debris thickness varies considerably. The objective of this study is to explore the factors that control the inter-glacier variability in surface thinning (dh) and surface mass balance (SMB) patterns of these two glaciers, with a view to advancing understanding of key mechanisms that control debris-covered glacier change in the southeastern Tibetan Plateau, and which may have relevance beyond this region of interest.

2 Study area

23K (~4 km^2) and 24K (~2 km^2) Glaciers are located in the southeastern Tibetan Plateau (~29.77° N, 95.70° E; Fig. 1). This region is characterized by steep and complex topography, as well as abundant precipitation, and has a glacierized area of ~10,000 km^2. Meltwater from glaciers in the region variously supply the Yarlung Tsangpo (the upper stream of the Brahmaputra River) and the Salween. These monsoon-dominated glaciers are characterized by high accumulation and high ablation rates (Shi et al., 2008). The region is mainly affected by two streams of humid air: the Bay of Bengal Vortex (in Spring) and the Indian Summer Monsoon system (in Summer), respectively (Ye and Gao, 1979; Yang et al., 2013; Yang et al., 2016). Thus, the monthly precipitation distribution exhibits a double-peak type occurring in both spring and summer (Yang et al., 2013). This is significantly different to the temporal patterns of mass gain on the Tibetan Plateau, which are so-called 'summer accumulation' type (Fujita et al., 2000; Maussion et al., 2014). Geodetic mass balance studies conducted at the regional scale indicate that the magnitude of recent ice loss in the region exceeds the average for High Mountain Asia (Kääb et al., 2012; Yao et al., 2012; Brun et al., 2017; Shean et al., 2020; Hugonnet et al., 2021), also affecting debris-

The Cryosphere
Discussions

covered glaciers. 23K and 24K Glaciers are located on the northern slopes of the Gangrigabu Mountains, ~23 kilometers and

24 kilometers, respectively, from Bomi City (Yang et al., 2017). 23K Glacier spans an altitudinal range of 3,760 to 5,437 m

100 a.s.l. and flows initially toward the south-east before turning to the northeast in the ablation zone (Fig. 1a). In contrast, 24K

Glacier flows to the northwest, and spans an altitudinal range of 3,900 to 5,621 m a.s.l. Both glaciers are partly covered by a

layer of rock debris (Fig. 1a, 1c) and the debris-covered area represents approximately 34% and 41% of the total area for

23K Glacier and 24K Glacier respectively. The terminus retreat patterns of the two glaciers are also conspicuously different;

terminus of 23K Glacier appears largely stagnant and is enclosed by a latero-terminal moraine complex, while the terminus

105 of 24K Glacier takes the form of a large ice cliff, and which is bounded by lateral moraines (Fig. 1c, 1d). Data from an

automatic weather station (AWS) on 24K Glacier indicates a warm and humid climate, with mean temperature and total

precipitation reaching ~9 °C and ~1700 mm, respectively between June and September (Yang et al., 2017; Fugger et al.,

2022).
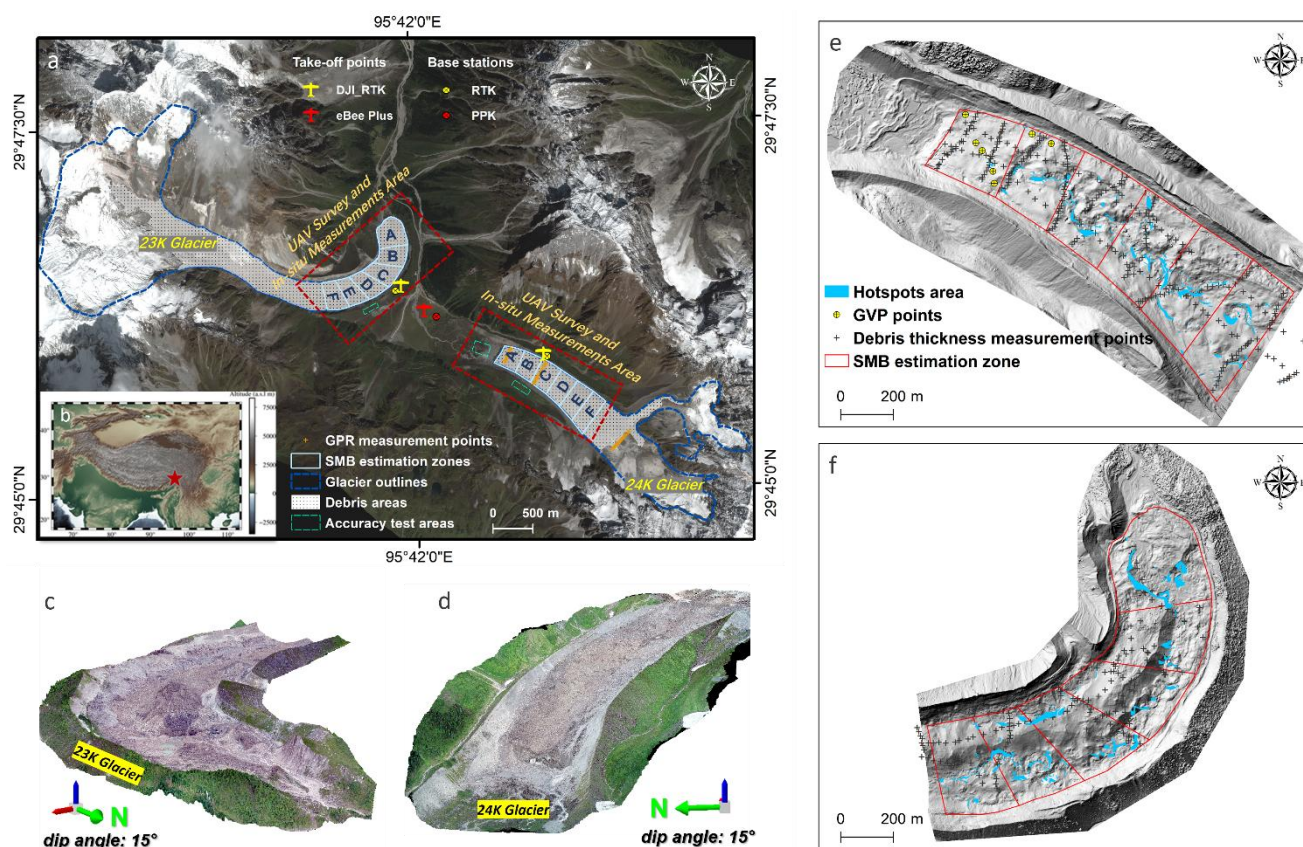
110   **Figure 1: (a) Overview of the 23K Glacier and 24K Glacier basin including the UAV survey area, accuracy test areas, *in-situ***
measurement locations (GVPs、GPR、debris thickness measurements), SMB estimation zones (zones A-F) and glacier outlines
(background image from Pléiades-1A false-color image from 2021-09-20). © CNES 2021, Distribution Airbus D&S. (b) Geographic
location of the study area. (c-d) UAV-derived three-dimensional images for the two glaciers. (e-f) Spatial distribution of the SMB
estimation zones of the two glaciers (e: 24K Glacier; f: 23K Glacier), debris thickness measurement points (in June 2019), and
115   **distribution of ice cliffs & supraglacial ponds (based on 2020 orthomosaics).**

3 Data and Method

3.1 UAV flights and data processing

Optical imagery of the glacier surface and its immediate surroundings was acquired using UAVs during four field campaigns that took place between August 13th 2019 and October 22nd 2020 (Table 1). We used an eBee Plus aircraft with built-in
120 GNSS PPK functionality in October 2019, August 2020, October 2020 surveys and DJI Phantom 4 RTK in August 2019 survey to capture the high-quality annua land seasonal pattern of glacier dynamics.

The eBee Plus (Fig.S1a) is a fixed-wing UAV that has a 20-megapixel RGB digital compact camera (SenseFly S.O.D.A.) The flight management software eMotion3® was used for flight planning. The DJI Phantom 4 RTK is a rotary-wing UAV (Fig.S1c) equipped with a 1-inch, 20-megapixel CMOS camera. In this study, all longitudinal and lateral image overlaps
125 were set to 65% and 80%, respectively. The flight lines for the eBee Plus and DJI Phantom 4 RTK maintained a relatively constant survey height above the glacier surface, which resulted in a constant ground resolution for each survey. A Huaxing A10 GNSS GPS was used as a static base station (Fig.S1b), and these data were attached to EXIF metadata of every geotagged image (Yang et al., 2020) and thereby integrated into a Post-Processed Kinematic (PPK) correction workflow to improve the accuracy of the UAV-SfM reconstruction. The DJI Phantom 4 real-time kinematic (RTK) UAV is permanently
130 connected to a GNSS receiver (D-RTK 2, Fig. S1d), so that each survey image already has its high-precision position information embedded (i.e., no post-processing required). The geotagged UAV images were used to create orthomosaics and DEMs using the SfM-based photogrammetric software Pix4Dmapper version 4.3.31.

Seven ground validation points (GVPs) were deployed during our UAV-SfM survey in October 2020 and their positions were measured with a dGPS system (section 3.2). By comparing the GVP measurements with the UAV-derived
135 orthomosaics and DEMs, we obtain absolute XYZ accuracies for the October 2020 UAV-SfM survey product (Table 2). While GVPs were not used for the other UAV-SfM surveys, the accuracies of all UAV-SfM products were indirectly assessed by comparing the horizontal (XY) and vertical (Z) errors between all orthomosaics and DEMs (Table 3). The horizontal (XY) error was estimated by measuring the displacements of 25 benchmark boulders located on stable off-glacier terrain. For the vertical (Z) error, we calculated the elevation difference over stable terrain, as outlined in Figure 1a.

Time	Flight type	Glacier	Number of Images	Flight altitude above ground (m)	Ground resolution (cm)	Coverage area (km^2)	Flight time (Beijing time)
13th Aug. 2019	RTK	23K	558	298	7.0	2.3	13:29-14:14
		24K	468	315	7.4	2.0	17:00-18:22
12th Oct. 2019	PPK	23K	743	243*	6.9	6.9	11:25-12:34
		24K	445				10:13-11:03
20th Aug. 2020	PPK	23K	128	434	10.2	3.1	12:07-12:26

The Cryosphere
Discussions
EGU
Open Access

		24K	160	536	12.6	3.7	11:11-11:35
22nd Oct. 2020	PPK	23K	188	344	8.1	2.4	10:37-10:59
		24K	346	374	8.8	3.8	8:57-9:37

Table 1: UAV photogrammetric flights used for acquisition of glacier image.

3.2 *In-situ* observations and measurements

To evaluate the role of debris on SMB patterns of both glaciers, debris thickness was manually measured by digging pits at selected sites in June 2019 (Fig. 1d, 1e). For 23K Glacier, a total of 157 locations were measured within the elevation range of 3,740-3,880 m a.s.l. For 24K Glacier, we measured a total of 349 points from the glacier terminus to 4,250 m a.s.l. The uncertainty in the manual measurement of the debris thickness was assumed to be 2 cm.

To assess the final positional accuracy of the UAV-derived DEMs and outputs, seven ground validation points (GVPs) were laid out in the vicinity of *in-situ* measurements (Fig.1a) on the surface of 24K Glacier in October 2020 (synchronized with the October 2020 UAV survey). We used a Huaxing A10 dGPS system to measure the position (XYZ) of each GVP. The horizontal accuracy of the dGPS is ± 8 mm and the vertical accuracy is ± 15 mm.

In October 2019, three ice thickness cross-sections (Fig.1a and Fig. S2) were measured on 24K Glacier using a Kentech ground penetrating radar (GPR) monopulse transmitter with 2.5 MHz antennas. The *in-situ* ice thickness measurements were used to correct the 24K Glacier distributed ice thickness dataset from Farinotti et al. (2019) (Fig. S2; Kneib et al., 2022). No *in-situ* ice thickness measurements exist for 23K Glacier; therefore, we directly used the consensus ice thickness from Farinotti et al. (2019) for this glacier.

In-situ observations from an on-glacier automatic weather station (AWS) in 24K Glacier (29.765° N, 95.713° E, 3900 m a.s.l.) was gathered for analysing air temperature differences between different survey periods.

3.3 Thinning (d*h*)，glacier dynamics and glacier driving stress

We compared the d*h* and velocity patterns of 23K and 24K Glaciers on an annual and on a seasonal timescale. The period between August 2019 and August 2020 (373 days, mean temperature of AWS: 1.66 °C) was selected for the annual timescale analysis. The annual rates were adjusted according to the ratio of days (366/373). For the seasonal analysis, we refer to the period October 2019-August 2020 (313 days, mean temperature: 0.42 °C) as the 'cold period' and the period August 2020-October 2020 (63 days, mean temperature: 8.68 °C) as the 'warm period'. For each period the thinning pattern was obtained by 2.5D DEM differencing in ArcGIS 10.4.

Glacier surface velocity is a good indicator of glacier dynamics (Kääb et al., 2003; Van, 2013) linked to the driving stress (e.g. Dehecq et al., 2019). A spatially distributed estimate of XY surface displacements was obtained for each period by

applying a Normalized Cross Correlation algorithm to the multidirectional 0.15 m-resolution DEM hillshades using ImGRAFT (Messerli and Grinsted, 2015). A search window of 10 × 10 pixels (1.5 × 1.5 m) was used to compute the magnitude and directions of the displacement vectors. We removed surface displacement values above 30 m (noise) and interpolated the surface velocity at these locations in ArcGIS 10.4 using nearest neighbors.

170 The glacier driving stress was calculated as (Cuffey and Paterson, 2010):

$$D_{stress} = \rho_i \cdot g \cdot h \cdot \sin \alpha_s, \tag{1}$$

where D_{stress} is the glacier driving stress, ρ_i is the density of ice (917 kg m³), g is the gravitational acceleration (9.81 m s⁻²), h is the ice thickness (in m), and α_s is the glacier slope obtained from the AW3D 30 m-resolution DEM (Tadono et al., 2014) smoothed with a Gaussian filter (8 pixels window). The consensus ice thickness product by Farinotti et al. (2019) is likely to

175 have large errors in the accumulation area of 24K glacier due to inaccurate RGI 6.0 glacier outlines that encompass the glacier headwall. However, in the ablation area, we applied a local correction using GPR measurements (section 3.2), which reduces the errors considerably.

3.4 Surface mass balance (SMB)

To investigate the magnitude and the distribution of the SMB, each glacier was divided into six zones (A-F) and each zone

180 was used as a separate section for the SMB estimation. Each SMB estimation zone was outlined manually, perpendicular to the main glacier flow line and with a similar area (Fig. 1a). To extract the melt contribution from the ice cliffs and ponds, we flow-corrected the DEMs following Brun et al. (2018). To perform the flow correction, we used orthomosaics and DEMs from the August 2020 UAV-SfM surveys as a reference for each glacier, to which the August 2019, October 2019 and October 2020 UAV-derived data were flow-corrected. Corrections in XY were made using the ArcGIS georeferencing tool

185 to manually track the surface flow for each given period by using surface tie points (mainly large boulders). For each correction period, the number of tie points was sufficiently large (> 75) and were well-distributed across the glacier surface to ensure a spatially representative correction, which took the form of a spline-based transformation. The resulting XY flow-corrected elevation change (dh_c, in m) is therefore equal to the sum of the surface mass balance ($\dot{b}$, negative value in the ablation area, in m) and mean vertical displacement (ω, in m):

190 $$dh_c = \dot{b} + \omega, \tag{2}$$

The ω can be expressed as:

$$\omega = \omega_s + \omega_e, \tag{3}$$

7

Where ω_s (in m) corresponds to the elevation change resulting from the horizontal flow-correction of the DEMs:

$$\omega_s = u_s \cdot tan\,(\alpha_m),\qquad(4)$$

195 Where u_s (in m) is the mean horizontal surface displacement and α_m (in °) is the mean surface slope of a given zone. ω_e (in m) corresponds to the flux divergence, which can be expressed as:

$$\omega_e = \frac{\Delta q}{A},\qquad(5)$$

Where A (in m²) is the area of the zone and Δq (in m³) is the ice flux difference at a given period:

$$\Delta q = q_{n+1} - q_n,\qquad(6)$$

200 Where q_{n+1} and q_n are the ice flux entering and leaving the estimation zone at a given period. q (in m³) is the ice flux through a glacier cross-section, given by:

$$q = \mu \cdot h_q \cdot v \cdot l,\qquad(7)$$

Where μ is a coefficient to convert the surface velocity into a depth-averaged velocity which we assumed to be equal to 0.9 following Miles et al. (2018), h_q (in m) is the ice thickness for the corresponding cross-section, v (in m) is the surface 205 displacement component normal to the cross sections line, l (in m) is the width of the cross-section.

The following equation was used to evaluate the uncertainty of SMB (σ_b) for each zone:

$$\sigma_b = \sqrt{\sigma_{dh_c}^2 + \sigma_\omega^2},\qquad(8)$$

The uncertainties of dh_c and u_s (also for v) were obtained by calculating the mean surface elevation difference and displacement the non-glacial test areas. They were determined as 0.09 m and 0.25 m respectively by averaging the values 210 over all periods.

The below equations were applied in the uncertainty of vertical component of velocity (σ_ω):

$$\sigma_\omega = \sqrt{\sigma_{u_s}^2 + \sigma_{\alpha_m}^2 + \sigma_{\omega_e}^2}\qquad(9)$$

Where:

The Cryosphere

Discussions

$$\frac{\sigma_{\omega_e}}{\omega_e} = \sqrt{\left(\frac{\sigma_{\Delta q}}{\Delta q}\right)^2 + \left(\frac{\sigma_A}{A}\right)^2}, \tag{10}$$

215 For the uncertainty associated with the slope correction, we assumed a 2° uncertainty in the slope (α_m). We assessed the uncertainty of zone area A by expanding the glacier area boundary by 20 m (Miles et al., 2016). The uncertainty of ice flux difference ($\sigma_{\Delta q}$):

$$\sigma_{\Delta q} = \sqrt{\sigma_{q_{n+1}}{}^2 + \sigma_{q_n}{}^2}, \tag{11}$$

σ_q (m³) is the uncertainty of ice flux through a glacier cross-section, given by:

220 $$\frac{\sigma_q}{q} = \sqrt{\left(\frac{\sigma_v}{v}\right)^2 + \left(\frac{\sigma_\mu}{\mu}\right)^2 + \left(\frac{\sigma_{h_q}}{h_q}\right)^2}, \tag{12}$$

Where the uncertainty of ratio μ (column-averaged velocity/surface velocity) is assumed as 0.1 (Cuffey and Paterson, 2010; Miles et al., 2018). The uncertainty in h_q is ~10-35 m (26%) for 23K Glacier (Farinotti et al., 2019) and is assumed to be equal to 12 m for the corrected 24K Glacier ice thickness uncertainty.

3.5 Ice cliffs and supraglacial ponds outlines and melt contribution

225 In this study, the proportion of ice cliffs and supraglacial ponds areas within each SMB estimation zone was calculated to better understand the SMB patterns on both glaciers during the ablation period. We manually extracted ice cliff and supraglacial pond outlines from the flow-corrected orthomosaics (August 2020 and October 2020; August 2019 and August 2020; October 2019 and August 2020). The outlines of the 'hotspots' area were obtained by merging two-phase outlines (Burn et al., 2018), and the total hotspots area for each zone was established by summing the area of these features. In this

230 way, we can effectively measure surface change in these hotspots zones, thereby providing us with an upper-bound estimate of the contribution of ice cliffs and ponds to the surface mass balance (Mishra et al., 2021; Kneib et al., 2022). We assumed the uncertainty of areas density of ice cliffs and supraglacial ponds to be equal to 0.5%.

4 Results

4.1 UAV products accuracy

235 The results from Oct. 2020 UAV-SfM products and GVPs measurements revealed that the mean absolute deviation in the X, Y and Z directions are 0.14 ± 0.11 m, 0.09 ± 0.11 m, and 0.24 ± 0.18 m respectively (Table 2). The vertical uncertainty is

twice as high as the horizontal uncertainty, which is in agreement with the findings of other studies (James et al., 2017; Li et al., 2019).

Table 2: XYZ geolocation accuracy of UAV-SfM orthomosaic and DEM (22nd Oct. 2020) for the two glaciers, based on the dGPS measurements of the 7 GVPs.

		X (m)	Y (m)	Z (m)
23K&24K	Mean	0.14	0.09	0.24
Glaciers	Std	0.11	0.11	0.18

The average XY errors for three survey pairs (Aug. 2019 *vs* Oct. 2019, Oct. 2019 *vs* Aug. 2020 and Aug. 2020 *vs* Oct. 2020) are 0.07 ± 0.06 m and 0.08 ± 0.06 m respectively (Table 3). The relative vertical (Z) errors between DEMs were ≤0.09 m for all pairs, which is appropriate for resolving fine-scale surface change for glaciological analysis.

Table. 3: XYZ errors between different orthomosaics/DEMs for the two glaciers using the fixed benchmark boulders and validation areas

|		23K&24K Glaciers		
		Aug. 2019-Oct. 2019	Oct. 2019-Aug. 2020	Aug. 2020-Oct. 2020
X (m)	Mean	0.07	0.08	0.07
	Std	0.06	0.07	0.06
Y (m)	Mean	0.06	0.09	0.09
	Std	0.04	0.06	0.05
Z (m)	Mean	0.09	0.08	0.09
	Std	0.07	0.04	0.08

4.2 Spatio-temporal variability of d*h* patterns

The d*h* distribution of different periods (annual, cold, warm) for the two glaciers is shown in Figure 2. The annual d*h* rate of the 23K Glacier in the survey area is -2.3 ± 0.1 m a^{-1}, whereas the d*h* rate of 24K Glacier is -1.2 ± 0.1 m a^{-1} (Fig. 2a, d). During the cold period (October 2019-August 2020), the average d*h* in the 23K (24K) Glacier survey area is -1.5 ± 0.1 m (-0.2 ± 0.1 m), with an average daily d*h* of -0.5 ± 0.03 cm d^{-1} (-0.1 ± 0.03 cm d^{-1}) (Fig. 2b, 2e). During the warm period (August 2020-October 2020), the mean d*h* for each glacier is more comparable to the other; for 23K (24K) Glacier it is -0.7 ± 0.1 m (-1.0 ± 0.1 m), with an average daily d*h* of -1.2 ± 0.03 cm d^{-1} (-1.6 ± 0.03 cm d^{-1}) (Fig. 2c, 2f).
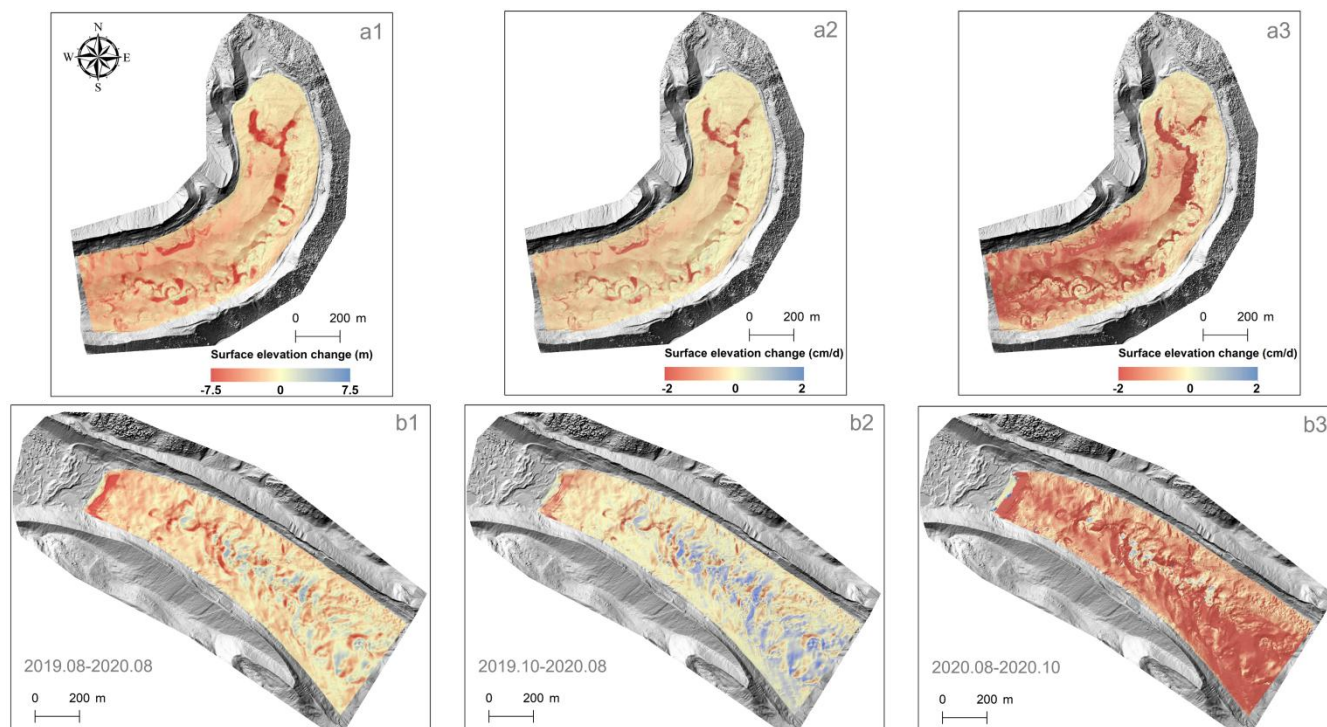
Figure 2: Annual surface elevation changes between UAV-derived DEMs for August 2019-August 2020 (a1, b1), the surface elevation change rates of the cold period (a2, b2) and the warm period (a3, b3) for the 23K Glacier (upper panels) and 24K Glacier (lower panels).

We present the relationships between dh rates and altitude for each glacier at 5 m and 15 m intervals (Fig 3). The relationships between dh rates and altitude show that the absolute dh of 23K Glacier increases with altitude (i.e., a negative gradient; ~-1 to -2 cm d^{-1} 100 m^{-1}) for every analysis period, while the dh of 24K Glacier decreases with altitude in the annual scale and cold period (positive gradient; ~+0.5 cm d^{-1} 100 m^{-1}). In particular, the dh-altitude gradient of 24K Glacier in the warm period follow the opposite trend to its annual scale and cold period's (i.e., consistent with 23K Glacier's), with the gradients of ~-2 cm d^{-1} 100 m^{-1} at 23K Glacier and ~-1 cm d^{-1} 100 m^{-1} at 24K Glacier (ignoring the effect of the terminal ice cliff).
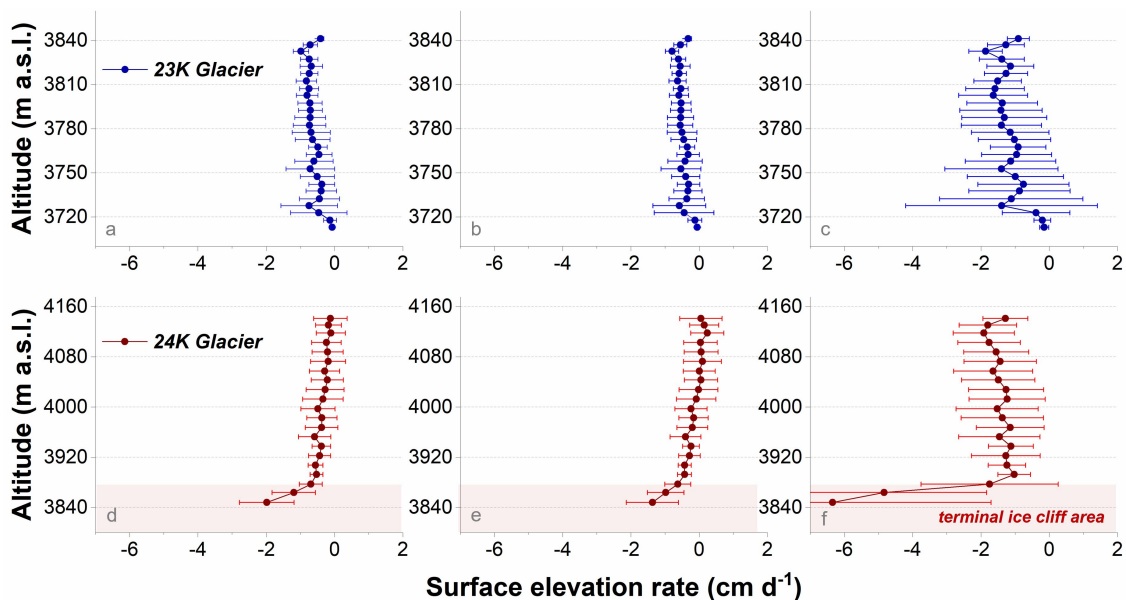
Figure 3: Annual average glacier surface elevation rates within 5-m (23K Glacier)/15-m (24K) elevation bands (dots) with the corresponding standard deviations (horizontal error bar) for August 2019-August 2020 (a, d), the cold period (b, e) and the warm period (c, f) across the monitoring area of the two glaciers. The red shadowed sections represent the terminal ice cliff at of the 24K Glacier.

4.3 Glacier dynamics

Between August 2019 and August 2020, the mean surface velocity is 1.7 ± 0.2 m a^{-1} for 23K Glacier and 9.2 ± 0.2 m a^{-1} for 24K Glacier (Fig. 4a1, a2). There is a zone of stagnation at the terminus of 23K Glacier where the surface velocity is less than 2 m a^{-1} (from terminus to 900 m up-glacier, Fig. 4a1). The mean surface velocities were also calculated for the cold and warm periods of both glaciers (Fig. 4b, 4c). During the cold period, the mean surface velocity of 23K Glacier is 0.4 ± 0.03 cm d^{-1}, while 24K Glacier is 2.4 ± 0.08 cm d^{-1}. During the warm period, the mean surface velocity for 23K Glacier and 24K Glacier are 0.6 ± 0.14 cm d^{-1} and 3.0 ± 0.40 cm d^{-1} respectively. For the UAV survey area, the mean driving stress of 23K Glacier is 1.6×10^5 Pa and for 24K Glacier is 2.1×10^5 Pa. The driving stress in the survey area for 24K Glacier is ~30% higher than for 23K Glacier (Fig. 4d). The estimated emergence velocities agree with the insight from surface velocities and driving stress, with 24K Glacier having significantly higher emergence velocities than 23K Glacier at any period (Fig. 4e). In this case, the annual emergence of 23K (24K) Glacier is 0.18 ± 0.04 m (1.36 ± 0.14 m), and 24K Glacier is approximately 7.6 times higher than 23K Glacier. The mean emergence of cold period for 23K (24K) Glacier is 0.16 ± 0.03 m (1.14 ± 0.11 m), the warm period emergence velocity for 23K (24K) Glacier is 0.07 ± 0.03 m (0.18 ± 0.04 m). The relationship between emergence and altitude for 23K Glacier was not remarkable for all periods, whereas the magnitude of emergence for 24K Glacier increased with altitude for all periods.
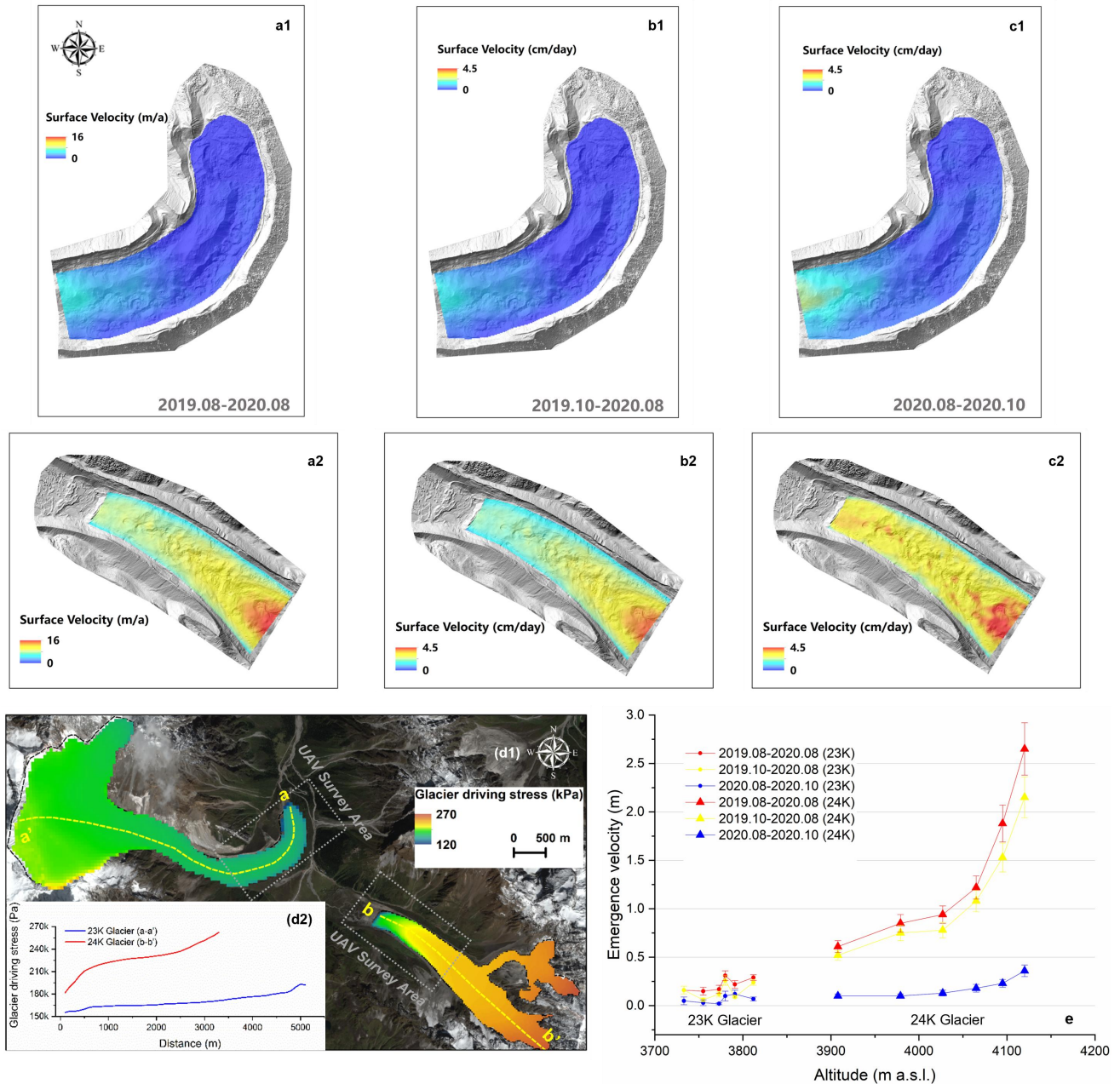
Figure 4: Average surface velocity for August 2019-August 2020 (a1, a2), the cold period (b1, b2) and the warm period (c1, c2). Spatial distribution of driving stresses (August 2019-August 2020) of the two glaciers (d1) and central flowlines (a-a' and b-b') driving stresses (d2), the grey dashed rectangular box (b1) represents the UAV aerial survey area, and we consider the confidence in the driving stress values of these parts to be higher than that of the upper part of the glacier, background image is a Pléiades-1A false-color image from 2021-09-20, which was used to derive the glacier outlines. © CNES 2021, Distribution Airbus D&S. The gradients between emergence velocity and altitude for two glaciers (e).

13

4.4 SMB patterns

At the annual scale, the mean SMB for 23K Glacier and 24K Glacier survey areas are -2.5 ± 0.1 m w.e. a^{-1} and -2.8 ± 0.3 m w.e. a^{-1} respectively and are therefore not significantly different (Fig. 5). During the 'cold' period, the glacier mass balance is -0.5 ± 0.03 cm w.e. d^{-1} for 23K Glacier and -0.4 ± 0.09 cm w.e. d^{-1} for 24K Glacier (Fig. 5). In contrast, during the warm
295   period, the mass balance of 23K Glacier is -1.3 ± 0.15 cm w.e. d^{-1}, while for 24K Glacier it is -1.9 ± 0.18 cm w.e. d^{-1}; the SMB during the warm period for 24K Glacier is thus ~46% higher than for 23K Glacier (Fig. 5). The SMB values of each mass balance zone (A-F) for both glaciers exhibit a weak decreasing trend with altitude in all periods (Fig. 6; Fig. S3).
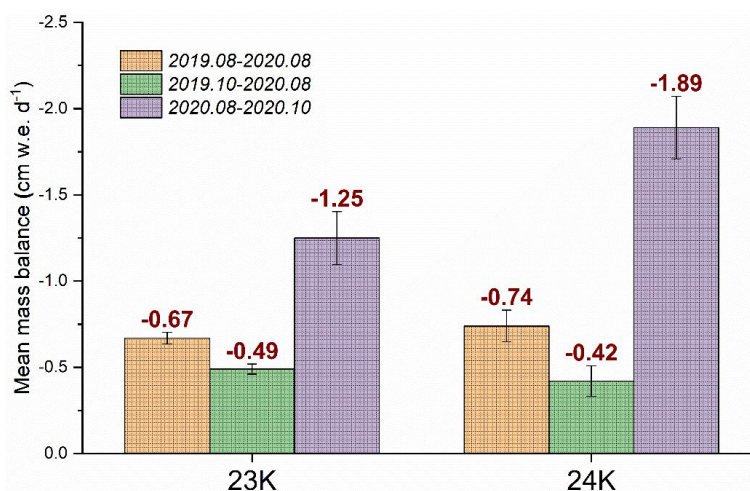

Figure 5: Mean SMB rates and their uncertainties for both UAV survey domains during the annual observation period (2019.08-
300   **2020.08), the cold period (2019.10-2020.08) and the warm period (2020.08-2020.10).**

The density of hotspots area for 23K Glacier is 6.8-7.2% and 4.4-5.1% for 24K Glacier (Table. 4). There are few ponds (~5, area > 100 m^2) on 23K Glacier, while there is no ponded area on 24K Glacier. Most ice cliffs on 24K Glacier are located in the center of the survey domain, while they are more homogeneously distributed on 23K Glacier (Fig. 1e, 1f). The average debris thickness in the UAV survey area of 23K Glacier and 24K Glacier is 47.1 ± 2 cm and 24.2 ± 2 cm respectively. The
305   debris thickness of both glaciers decreases with increasing altitude in the UAV survey area (23K Glacier: ~ -57 cm 100 m^{-1}; 24K Glacier: ~ -9 cm 100 m^{-1}). To disentangle the influence of the sub-debris area and the hotspots area for the SMB pattern respectively, we extracted the SMB rates of hotspots area and sub-debris area in both glaciers for all periods (Table. 4). As shown in Table 4, the SMB rates in the hotspots area of both glaciers are higher than the sub-debris area during all periods (i.e., the hotspots area possess the higher melt efficiency). The enhancement factor was calculated to quantify such difference
310   in melt efficiency between two glaciers' hotspots area and sub-debris area during all periods, which we define as the ratio of the hotspots area SMB rate to the sub-debris area SMB rate (Brun et al., 2018, Buri et al., 2021, Miles et al., 2022). In this study, the enhancement factors for the two glaciers range from 1.6 to 4.4 during all periods. It is also found that enhancement

factors were consistently higher in 23K Glacier than in 24K Glacier (~1.5-1.8 times). The enhancement factors for the two glaciers are significantly higher in the warm period than in the annual scale (23K: ~2.0 times；24K: ~1.6 times) and cold period (23K: ~1.7 times；24K: ~1.5 times), indicating that the 'hotspots effect' is more pronounced during the ablation period.

Table 4: Hotspots area proportion, mean hotspots area and sub-debris area SMB, hotspots area enhancement factors in all periods for both glaciers.

Time	Glacier	Hotspots area proportion (%)	Mean hotspots area SMB (cm w.e. d^{-1})	Mean sub-debris area SMB (cm w.e. d^{-1})	Hotspots area enhancement factors (-)
Aug. 2019-Aug. 2020	23K	6.8 ± 0.5	-1.3 ± 0.03	-0.6 ± 0.03	2.2
	24K	5.1 ± 0.5	-1.1 ± 0.1	-0.7 ± 0.1	1.6
Oct. 2019-Aug. 2020	23K	7.1 ± 0.5	-1.1 ± 0.03	-0.4 ± 0.03	2.6
	24K	4.9 ± 0.5	-0.7 ± 0.1	-0.4 ± 0.1	1.7
Aug. 2020-Oct. 2020	23K	7.2 ± 0.5	-4.1 ± 0.2	-0.9 ± 0.2	4.4
	24K	4.4 ± 0.5	-4.4 ± 0.2	-1.7 ± 0.2	2.6

To better disentangle the effects of debris thickness and hotspots areas on glaciers melt, we compared the mean debris thickness, the percentage of ice cliff and supraglacial ponds area and the mean melt rate in warm period in each of the six zones (A-F) of each glacier (Fig. 6). We assessed the correlations of the zonal SMB in warm period with the zonal debris thickness and ice cliffs and supraglacial ponds density based on six points for each glacier. For 23K Glacier, the correlation coefficient, r, between debris thickness and SMB during the warm period is 0.88 (p = 0.02), indicating that the debris thickness is highly correlated with the melt. In contrast, the correlation coefficient between the percentage of ice cliff and supraglacial ponds area, and the SMB, is -0.29 (p = 0.58), indicating the absence of a strong correlation. During the warm period, 24K Glacier exhibits a strong relationship between the debris thickness and melt, where r is 0.82 (p = 0.05). Hotspots area is weakly correlated with the glacier melt (r = -0.48, p = 0.36).
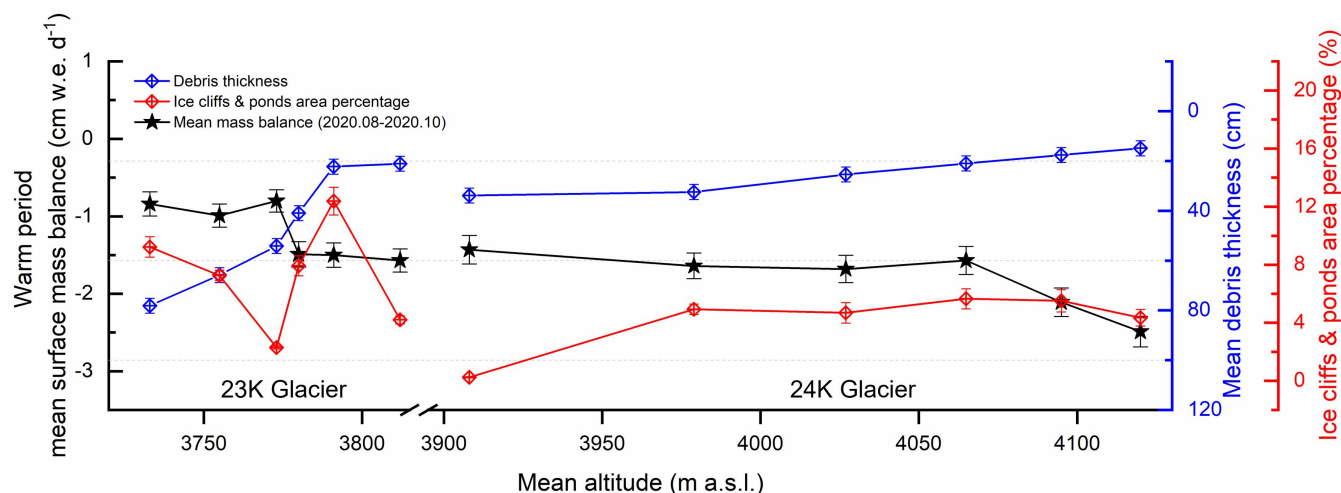
Figure 6: The daily SMB and during the warm period (black solid line), the mean debris thickness (blue solid line) and the mean percentage of the ice cliffs and supraglacial ponds area (red solid line) for the individual zones of two glaciers.

5 Discussion

5.1 Controls of the d*h* patterns

The d*h* patterns of the two glaciers are very different at annual scale and during cold period, as indicated by its magnitude and spatial distribution. The annual d*h* rate of 23K Glacier is approximately twice than that of the 24K Glacier, but the rate at which SMB evolves with altitude exhibits less variation between two glaciers (Fig. 6, Figure S3). These large difference in d*h* between two glaciers are mainly caused by different dynamic states (Fig. 4; Brun et al., 2018; Anderson et al., 2021a, 2021b; Rounce et al., 2021). In this study, the emergence velocity replenishment is consistently higher on 24K Glacier than on 23K Glacier in any period (Fig. 4e), and the estimated surface velocities and driving stress results support this conclusion (Fig. 4a, b, c, d). The dynamic state of a glacier is a clear indicator of its health (Miles et al., 2021), and this study illustrates that glacier health can vary greatly even over small distances. 23K and 24K Glaciers may be thought to experience the same climatic forcing, yet their distinct geometry, and possibly distinctive dependence on avalanche and rockfall mass supply, has led to marked differences in mass supply to the glacier terminus. However, the d*h* magnitude and spatial distribution of 24K Glacier are similar to that of 23K Glacier during the warm period (Fig. 2, Fig. 3), due to the fact that the ablation determines the d*h* pattern and dilutes the emergence velocity contribution of 24K Glacier during this period. For 23K Glacier, the ablation consistently determines its d*h* patterns due to the weak emergence velocity replenishment during all periods (Fig. 4e).

To better evaluate the role of emergence velocity replenishment on d*h*, we calculated the ratio of emergence velocity to SMB (Table. 5). The greater of the absolute value of this ratio indicates the greater impact of emergence velocity replenishment on

16

d*h*. The ratio of annual emergence velocity and annual SMB for 23K (24K) Glacier is -0.09 (-0.49). The ratio values for 23K

350   (24K) Glacier during cold and warm periods are -0.11 (-0.87) and -0.09 (-0.15), respectively. The ratio absolute values for
24K Glacier are always higher than those for 23K Glacier, especially evident in the non-ablation period. Hence, the survey
area on 23K Glacier is weakly replenished by the upstream ice flux while the stronger upstream ice flux for 24K Glacier
serves to restrain the annual surface thinning signal (Fig.4). Fu et al. (2022) also conducted d*h* observations for a debris-
covered glacier (Hailuogou Glacier) in the southeastern Tibetan Plateau. They revealed that the tongue area showed a

355   considerable d*h* (-2.81 m) during an ablation period and that its dynamic state is very weak, similar to what we observe for
23K Glacier. Other studies concerning the mass balance of Himalayan debris-covered glaciers also report on glaciers which
possess a high d*h* rate (~-0.9-1.8 m a^{-1}) and weaker dynamic state (Vincent et al., 2016; Nuimura et al., 2017; Brun et al.,
2018; Rowan et al., 2021), and which possess d*h* patterns which are consistent with that of 23K Glacier. In summary, the d*h*
pattern for 23K Glacier appears to conform to that of other Himalayan debris-covered glaciers, whilst that of 24K Glacier is

360   exceptional is perhaps more anomalous.

Table 5: Emergence velocity, SMB and the ratio of above two in all periods for both glaciers.

Time	Glacier	Emergence velocity (m w.e.)	SMB (m w.e.)	Ratio of emergence velocity to SMB
Aug. 2019-Aug. 2020	23K	0.22 ± 0.04	-2.50 ± 0.11	-0.09
	24K	1.36 ± 0.14	-2.76 ± 0.34	-0.49
Oct. 2019-Aug. 2020	23K	0.16 ± 0.03	-1.53 ± 0.09	-0.11
	24K	1.14 ± 0.11	-1.31 ± 0.25	-0.87
Aug. 2020-Oct. 2020	23K	0.07 ± 0.03	-0.79 ± 0.09	-0.09
	24K	0.18 ± 0.04	-1.19 ± 0.11	-0.15

Field observations show that the terminus type differs between each glacier (Fig. 1c, 1d, Fig S4). These differences likely
reflect this difference in ice dynamics and emphasize their contrasting position within the glacier-debris-covered glacier-rock
glacier continuum (Anderson et al., 2018). The terminus of 23K Glacier is largely stagnant with a low d*h* rate, a suppressed

365   dynamic state, and the presence of supraglacial ponds which, combined, are consistent with observations of stagnating
debris-covered glaciers in other glacierised regions globally (e.g., Benn et al, 2012). In contrast, 24K Glacier has a steep
longitudinal gradient with a smooth surface and has developed a sizable terminal ice cliff (Fig. S4); this feature, where mass
is lost due to progressive melt, and episodic 'dry' calving promotes glacier retreat. Such terminal-cliff debris-covered
glaciers are less well studied but have been noted in a variety of settings (e.g., Ferguson and Vieli, 2021). Terminus type can

370   have an important influence on debris-covered glacier geometry (Anderson et al., 2016) and may thus influence glacier
geometric evolution in a warming climate. Our investigations suggest that 24K Glacier exhibits reduced climatic-geometric
imbalance than 23K Glacier, possibly because it has responded to climate warming with progressive retreat.

5.2 Possible reasons for SMB patterns

The existence of a debris cover and its influence on ablation typically causes SMB patterns for debris-covered glaciers to
375 differ from those of largely debris-free glaciers (Ostrem, 1959; Nakawo et al., 1999; Nicholson and Benn, 2006; Reid and
Brock, 2010; Yang et al., 2017), and our results show inverted melt-season SMB profiles for both 23K and 24K Glaciers. In
addition, debris-covered glaciers tend to develop ice cliffs and supraglacial ponds which enhance melt locally, even relative
to clean ice (Sakai, 1998, 2002; Reid and Brock, 2014; Juen et al., 2014; Steiner et al., 2015; Buri et al., 2016, 2021; Miles et
al., 2016, 2018, 2022; Kneib et al., 2022). Overall, the annual SMB of 23K Glacier and 24K Glacier are similar, but the rate
380 of mass loss is higher for 24K Glacier during the warm period. During all periods, the magnitude of ablation increases with
elevation for both glaciers, with the same spatial distribution (Fig. 6, Fig. S3). We find that the correlation between the melt
and the debris thickness distribution is strong for both glaciers during the warm period, while there is little correlation
between the melt and the hotspots area distribution.

With the relationship between SMB and debris thickness established for the two glaciers during the ablation period, we
385 found that the mean residuals sourced from SMB-debris thickness relationship of 23K Glacier were larger than the 24K
Glacier (47.1 *vs* 24.2). Although there is no clear correlation between SMB and hotspots, the above nearly double residual
difference is hypothesized to be based on the large difference in hotspots area enhancement factors of two glaciers (23K: 4.4,
24K: 2.6; ~1.7 times). It reflects some of the influence of hotspots area on SMB/melt patten. By extracting the ablation
contribution of the ice cliffs and supraglacial ponds (Fig. 7), we found that the total melt from hotspots areas accounted for
390 $31.5 \pm 2.2\%$ of the total melt in the UAV survey area. For 24K Glacier, the ablation in hotspots areas accounts for $11.4 \pm$
1.3% of the total melt in the survey area for this glacier. Based on UAV and time-lapse camera observations, Kneib et al.
(2022) carried out high-precision observation of a single ice cliff on the 24K Glacier, and the daily cliff melt during the
ablation period is 3.9-5.1 cm day^{-1}. In this study, the daily melt of the 24K Glacier hotspots areas during warm period was
estimated to be 4.4 ± 0.2 cm w.e. d^{-1} (~4.9 cm day^{-1}), which is similar to the observed value for a single ice cliff. The role of
395 hotspots area is not negligible, as glacier ablation would be underestimated by $24.5 \pm 1.7\%$ and $7.0 \pm 0.7\%$, respectively, if
the hotspots areas were not taken into account when carrying out the two glaciers mass balance modelling work. Other
studies have observed and simulated the contribution of ice cliffs to be 17-26% of total ablation, which is in agreement with
our results (Brun et al., 2018; Anderson et al., 2021a; Buri et al., 2021). However, the areal proportion of hotspots areas
(23K Glacier: 7.2 ± 0.5 %, 24K Glacier: 4.4 ± 0.5 %) is much smaller than that of the sub-debris melt area for each glacier.
400 This has the overall effect that enhanced melt in these regions does not have a marked effect on glacier-scale SMB profiles,
but rather leads to an increase in ablation throughout the debris-covered area. We note that in this study the outlines of
hotspots area as digitized for warm periods were obtained based on the merged outlines (Brun et al., 2018), which may lead
to an overestimation of the extent of the hotspots area (Kneib et al., 2022). In other words, the actual hotspots area may
represent a lower proportion of the UAV survey area. Though the hotspots area is recognized as local controls of melt

18

405   patterns, the debris thickness is the dominant altitudinal control the glacier scale for 23K Glacier and 24K Glacier, similar to the conclusion at Kennicott Glacier in Alaska (Anderson et al, 2021a).
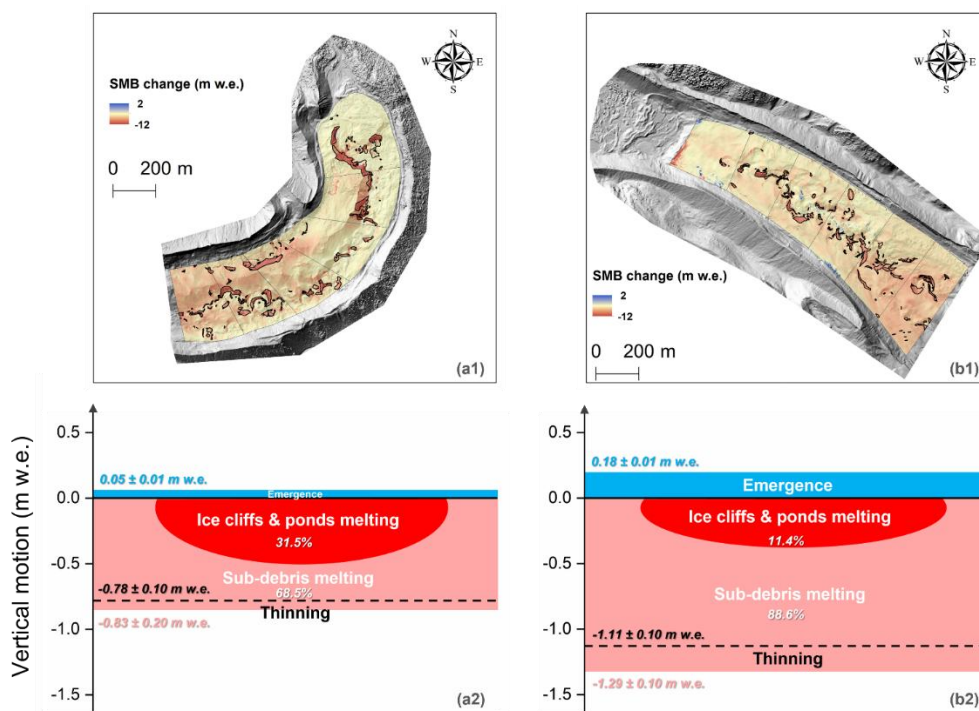

Figure 7: Spatial distribution of surface mass balance during ablation period for the UAV survey domains of 23K Glacier and 24K Glacier (a1, b1). The a2 and b2 are the conceptual diagrams of vertical motion components for 23K Glacier and 24K Glacier.

410   In this study, it gives us insight into the clear controlling role of the debris on melt pattern. In future research, it is beneficial to improve our understanding of the responses of debris-covered glaciers to climate change to focus the debris supply and evacuation differences etc. According to field photography (Fig. S5), we also found that paraglacial slope failure (PSF) events have occurred in the catchment of 23K Glacier recently and may be the result of complex interactions between geologic structure and stress-related slope response to glacier mass loss (Zhong et al., 2022). Such events may become an

415   increasingly important component of the debris supply and transport cascade for these land systems, with implications for the future development of supraglacial debris cover, glacier mass balance, and flow dynamics; large rock avalanches which emplace in supraglacial environments have led to melt suppression and glacier advance in other locations (e.g., McSaveney, 1975; Shugar and Clague, 2011), and, if sufficiently thick, this event could thus temporarily rejuvenate the emergence velocity into the terminus area.

19

The Cryosphere
Discussions

Open Access

EGU

5.3 Glaciers change in the early twenty-first century

420

The thinning of 23K Glacier tongue is greater than that of 24K Glacier since 2000 (Hugonnet et al., 2021; Fig. 8), which is generally in agreement with the current d*h* pattern. It is found that the thinning rates of both glaciers show the accelerated increase over the last two decades (23K: +77%; 24K: +100%). However, the increase rate of 24K Glacier tongue is slightly lower than that of 23K Glacier over the last decade (23K: +44%; 24K: +20%).
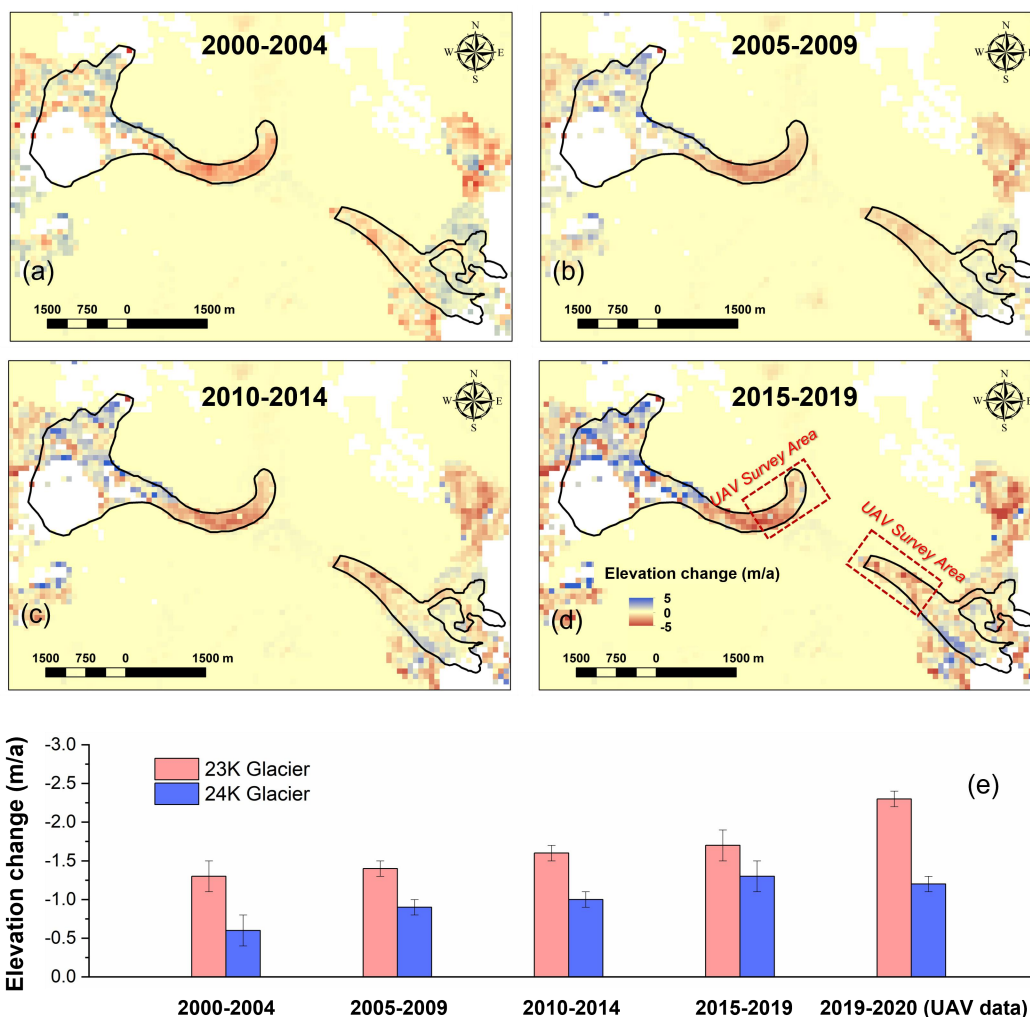
425

Figure 8: Annual surface elevation changes for 2000-2004 (a), 2005-2009 (b), 2010-2014 (c), 2015-2019(d) for the 23K Glacier and 24K Glacier (red dashed rectangular box represents the UAV aerial survey area). Annual surface elevation changes and their uncertainties for both UAV survey domains at different periods (e).

We explore the glaciers dynamic state change by analysing the surface velocities over the last two decades (Dehecq et al.,

430 2015; Fig. 9). It is found that the surface velocities of both glaciers decreased significantly in the first fifteen years of this century with the surface velocities of 1999-2003 and 2013-2015. During this period, 23K and 24K Glaciers decrease by 84%

and 54% respectively. In contrast, there is no clear decreasing trend in the surface velocity of two glaciers in the last five years (2015-2020). The 24K Glacier tongue is still replenished by ice flux at present, which compensates for its higher melt due to its thinner debris thickness. It is necessary for 24K Glacier to carry out continuous, high-precision surface velocity

435 observations to understand its future fate.

The mean SMB for both UAV survey domains from 2000-2016 were -1.5 ± 0.7 m w.e. a^{-1} and -1.6 ± 1.1 m w.e. a^{-1} (Miles et al., 2021), they are lower than the magnitude of SMB in 2019-2020, which is mainly driven by the global warming. From 2000-2016, the magnitude of SMB was slightly greater on 24K Glacier than on 23K Glacier, which is similar with the recent SMB results (2019-2020) derived from the UAV data.
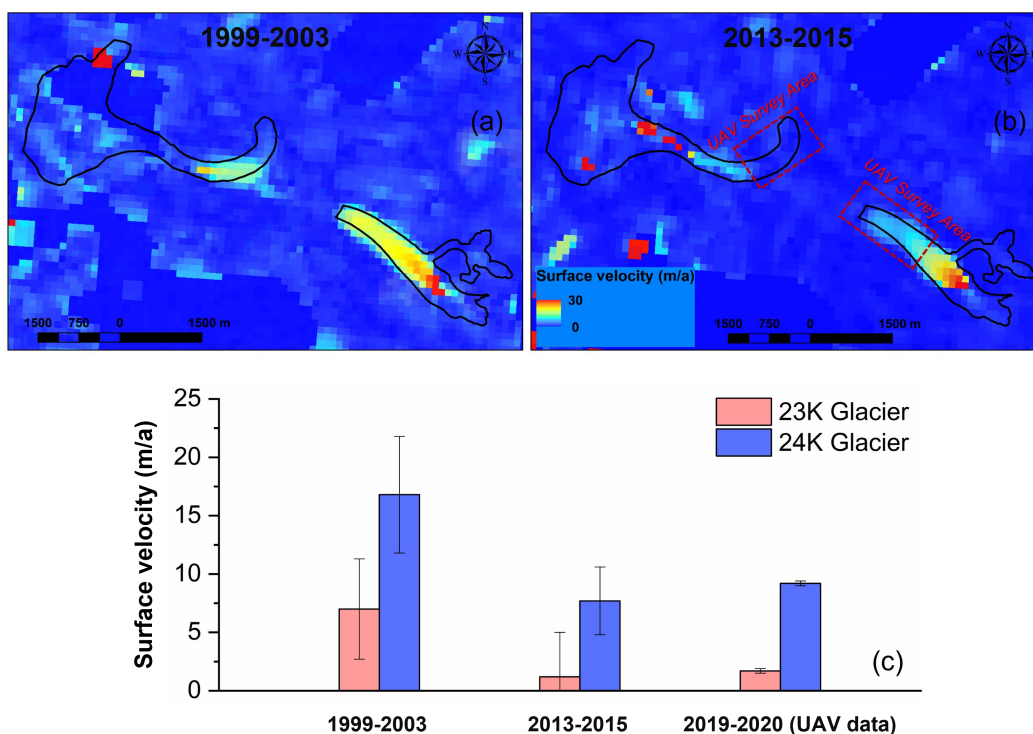
440

Figure 9: Annual surface velocity for 1999-2003 (a), 2013-2015 (b) for the 23K Glacier and 24K Glacier (red dashed rectangular box represents the UAV aerial survey area). Annual surface velocities and their uncertainties for both UAV survey domains at different periods (c).

Conclusions

445 We have used multi-temporal high-resolution UAV-SfM surveys combined with *in-situ* observations to quantify thinning (d*h*) and surface mass balance (SMB) patterns of two neighboring, but contrasting, debris-covered glaciers in the southeastern Tibetan Plateau. The conclusions are summarized as follows：

1) The dh patterns of the two glaciers display distinct characteristics at annual scale. The annual dh of 23K Glacier UAV survey area is 1.9 times greater than that of 24K Glacier. The magnitude of 23K Glacier dh increases with altitude, similar to many other debris-covered glaciers, whereas 24K Glacier shows the opposite pattern, except during the melt season. These contrasting patterns are mainly driven by the stronger dynamic state of 24K Glacier, which has a much higher downward emergence velocity replenishment.

2) The SMB patterns of the two glaciers are generally in agreement. The magnitude of SMB on both glaciers increases with altitude in the ablation period, exhibiting melt inversion which is attributable to the debris thickness distribution (which decreases with altitude). Due to the low areal proportion of ice cliffs and supraglacial ponds area (melt hotspots), sub-debris ablation accounts for the majority of the total ablation. Debris thickness variations show a clear control on zonal SMB. The cliffs and ponds melt enhancement factor which ranges between 2.6 and 4.4 during warm period, hotspots area's melt contribution is still considerable.

3) Both glaciers experience accelerated thinning and their surface velocities are decreased by analysing the elevation and surface velocity changes over the last two decades. 23K Glacier possesses the higher dh rate and its dynamic state is weaker than the 24K Glacier. The magnitude of the annual SMB for both glaciers in 2000-2016 is lower than the 2019-2020 results (from UAV data), but 24K Glacier is consistently slightly higher than 23K Glacier.

4) Such a high-resolution and comparative observation gives a rare perspective into the controls of the thinning and melt of debris-covered glacier. We provide evidence that the rate of mass loss on such glaciers can be highly dependent on dynamic state, and that the relatively thin debris on these glaciers is the main control of the glacier surface ablation patterns, with supraglacial cliffs and ponds primarily serving to enhance mass loss.

References

Allen, S. K., Zhang, G. Q., Wang, W. C., Yao, T. D., and Bolch, T.: Potentially dangerous glacial lakes across the Tibetan Plateau revealed using a large-scale automated assessment approach, Science Bulletin, 64, 435-445, 10.1016/j.scib.2019.03.011, 2019.

An, B. S., Wang, W. C., Yang, W., Wu, G. J., Guo, Y. H., Zhu, H. F., Gao, Y., Bai, L., Zhang, F., Zeng, C., Wang, L., Zhou, J., Li, X., Li, J., Zhao, Z. J., Chen, Y. Y., Liu, J. S., Li, J. L., Wang, Z. Y., Chen, W. F., and Yao, T. D.: Process, mechanisms, and early warning of glacier collapse-induced river blocking disasters in the Yarlung Tsangpo Grand Canyon, southeastern Tibetan Plateau, Science of the Total Environment, 816, 10.1016/j.scitotenv.2021.151652, 2022.

Anderson, L. S. and Anderson, R. S.: Debris thickness patterns on debris-covered glaciers, Geomorphology, 311, 1-12, 10.1016/j.geomorph.2018.03.014, 2018.

Anderson, L. S., Armstrong, W. H., Anderson, R. S., and Buri, P.: Debris cover and the thinning of Kennicott Glacier, Alaska: in situ measurements, automated ice cliff delineation and distributed melt estimates, Cryosphere, 15, 265-282, 10.5194/tc-15-265-2021, 2021a.

Anderson, L. S., Armstrong, W. H., Anderson, R. S., Scherler, D., and Petersen, E.: The Causes of Debris-Covered Glacier Thinning: Evidence for the Importance of Ice Dynamics From Kennicott Glacier, Alaska, Frontiers in Earth Science, 9, 10.3389/feart.2021.680995, 2021b.

Bash, E. A. and Moorman, B. J.: Surface melt and the importance of water flow - an analysis based on high-resolution unmanned aerial vehicle (UAV) data for an Arctic glacier, Cryosphere, 14, 549-563, 10.5194/tc-14-549-2020, 2020.

Benn, D. I., Bolch, T., Hands, K., Gulley, J., Luckman, A., Nicholson, L. I., Quincey, D., Thompson, S., Toumi, R., and Wiseman, S.: Response of debris-covered glaciers in the Mount Everest region to recent warming, and implications for outburst flood hazards, Earth-Science Reviews, 114, 156-174, 10.1016/j.earscirev.2012.03.008, 2012.

Benoit, L., Gourdon, A., Vallat, R., Irarrazaval, I., Gravey, M., Lehmann, B., Prasicek, G., Graff, D., Herman, F., and Mariethoz, G.: A high-resolution image time series of the Gorner Glacier - Swiss Alps - derived from repeated unmanned aerial vehicle surveys, Earth System Science Data, 11, 579-588, 10.5194/essd-11-579-2019, 2019.

Brun, F., Berthier, E., Wagnon, P., Kaab, A., and Treichler, D.: A spatially resolved estimate of High Mountain Asia glacier mass balances from 2000 to 2016, Nature Geoscience, 10, 668-+, 10.1038/ngeo2999, 2017.

Brun, F., Buri, P., Miles, E. S., Wagnon, P., Steiner, J., Berthier, E., Ragettli, S., Kraaijenbrink, P., Immerzeel, W. W., and Pellicciotti, F.: Quantifying volume loss from ice cliffs on debris-covered glaciers using high-resolution terrestrial and aerial photogrammetry, Journal of Glaciology, 62, 684-695, 10.1017/jog.2016.54, 2016.

Brun, F., Wagnon, P., Berthier, E., Shea, J. M., Immerzeel, W. W., Kraaijenbrink, P. D. A., Vincent, C., Reverchon, C., Shrestha, D., and Arnaud, Y.: Ice cliff contribution to the tongue-wide ablation of Changri Nup Glacier, Nepal, central Himalaya, Cryosphere, 12, 3439-3457, 10.5194/tc-12-3439-2018, 2018.

Brun, F., Wagnon, P., Berthier, E., Jomelli, V., Maharjan, S. B., Shrestha, F., and Kraaijenbrink, P. D. A.: Heterogeneous Influence of Glacier Morphology on the Mass Balance Variability in High Mountain Asia, Journal of Geophysical Research-Earth Surface, 124, 1331-1345, 10.1029/2018jf004838, 2019.

Buri, P., Miles, E. S., Steiner, J. F., Immerzeel, W. W., Wagnon, P., and Pellicciotti, F.: A physically based 3-D model of ice cliff evolution over debris-covered glaciers, Journal of Geophysical Research-Earth Surface, 121, 2471-2493, 10.1002/2016jf004039, 2016.

Buri, P., Miles, E. S., Steiner, J. F., Ragettli, S., and Pellicciotti, F.: Supraglacial Ice Cliffs Can Substantially Increase the Mass Loss of Debris-Covered Glaciers, Geophysical Research Letters, 48, 10.1029/2020gl092150, 2021.

Cao, B., Guan, W. J., Li, K. J., Pan, B. T., and Sun, X. D.: High-Resolution Monitoring of Glacier Mass Balance and Dynamics with Unmanned Aerial Vehicles on the Ningchan No. 1 Glacier in the Qilian Mountains, China, Remote Sensing, 13, 10.3390/rs13142735, 2021.

Dehecq, A., Gourmelen, N., and Trouve, E.: Deriving large-scale glacier velocities from a complete satellite archive: Application to the Pamir-Karakoram-Himalaya, Remote Sensing of Environment, 162, 55-66, 10.1016/j.rse.2015.01.031, 2015.

Dehecq, A., Gourmelen, N., Gardner, A. S., Brun, F., Goldberg, D., Nienow, P. W., Berthier, E., Vincent, C., Wagnon, P., and Trouve, E.: Twenty-first century glacier slowdown driven by mass loss in High Mountain Asia, Nature Geoscience, 12, 22-+, 10.1038/s41561-018-0271-9, 2019.

Farinotti, D., Huss, M., Furst, J. J., Landmann, J., Machguth, H., Maussion, F., and Pandit, A.: A consensus estimate for the ice thickness distribution of all glaciers on Earth, Nature Geoscience, 12, 168-+, 10.1038/s41561-019-0300-3, 2019.

Ferguson, J. C. and Vieli, A.: Modelling steady states and the transient response of debris-covered glaciers, Cryosphere, 15, 3377-3399, 10.5194/tc-15-3377-2021, 2021.

Fu, Y., Liu, Q., Liu, G. X., Zhang, B., Zhang, R., Cai, J. L., Wang, X. W., and Xiang, W.: Seasonal ice dynamics in the lower ablation zone of Dagongba Glacier, southeastern Tibetan Plateau, from multitemporal UAV images, Journal of Glaciology, 10.1017/jog.2021.123,

Fugger, S., Fyffe, C. L., Fatichi, S., Miles, E., McCarthy, M., Shaw, T. E., Ding, B. H., Yang, W., Wagnon, P., Immerzeel, W., Liu, Q., and Pellicciotti, F.: Understanding monsoon controls on the energy and mass balance of glaciers in the Central and Eastern Himalaya,

520   Cryosphere, 16, 1631-1652, 10.5194/tc-16-1631-2022, 2022.

Fujita, K. and Ageta, Y.: Effect of summer accumulation on glacier mass balance on the Tibetan Plateau revealed by mass-balance model, Journal of Glaciology, 46, 244-252, 10.3189/172756500781832945, 2000.

Gardelle, J., Berthier, E., Arnaud, Y., and Kaab, A.: Region-wide glacier mass balances over the Pamir-Karakoram-Himalaya during 1999-2011, Cryosphere, 7, 1263-1286, 10.5194/tc-7-1263-2013, 2013.

525   Gibson, M. J., Glasser, N. F., Quincey, D. J., Mayer, C., Rowan, A. V., and Irvine-Fynn, T. D. L.: Temporal variations in supraglacial debris distribution on Baltoro Glacier, Karakoram between 2001 and 2012, Geomorphology, 295, 572-585, 10.1016/j.geomorph.2017.08.012, 2017.

Hambrey, M. J., Quincey, D. J., Glasser, N. F., Reynolds, J. M., Richardson, S. J., and Clemmens, S.: Sedimentological, geomorphological and dynamic context of debris-mantled glaciers, Mount Everest (Sagarmatha) region, Nepal, Quaternary Science Reviews, 27, 2361-2389,

530   10.1016/j.quascirev.2008.08.010, 2008.

Herreid, S. and Pellicciotti, F.: The state of rock debris covering Earth's glaciers, Nature Geoscience, 13, 621, 10.1038/s41561-020-0615-0, 2020.

Hugenholtz, C. H., Whitehead, K., Brown, O. W., Barchyn, T. E., Moorman, B. J., LeClair, A., Riddell, K., and Hamilton, T.: Geomorphological mapping with a small unmanned aircraft system (sUAS): Feature detection and accuracy assessment of a

535   photogrammetrically-derived digital terrain model, Geomorphology, 194, 16-24, 10.1016/j.geomorph.2013.03.023, 2013.

Hugonnet, R., McNabb, R., Berthier, E., Menounos, B., Nuth, C., Girod, L., Farinotti, D., Huss, M., Dussaillant, I., Brun, F., and Kaab, A.: Accelerated global glacier mass loss in the early twenty-first century, Nature, 592, 726-+, 10.1038/s41586-021-03436, 2021.

Immerzeel, W. W., Kraaijenbrink, P. D. A., Shea, J. M., Shrestha, A. B., Pellicciotti, F., Bierkens, M. F. P., and de Jong, S. M.: High-resolution monitoring of Himalayan glacier dynamics using unmanned aerial vehicles, Remote Sensing of Environment, 150, 93-103,

540   10.1016/j.rse.2014.04.025, 2014.

James, M. R., Robson, S., and Smith, M. W.: 3-D uncertainty-based topographic change detection with structure-from-motion photogrammetry: precision maps for ground control and directly georeferenced surveys, Earth Surface Processes and Landforms, 42, 1769-1788, 10.1002/esp.4125, 2017.

Juen, M., Mayer, C., Lambrecht, A., Han, H., and Liu, S.: Impact of varying debris cover thickness on ablation: a case study for Koxkar

545   Glacier in the Tien Shan, Cryosphere, 8, 377-386, 10.5194/tc-8-377-2014, 2014.

Kaab, A., Berthier, E., Nuth, C., Gardelle, J., and Arnaud, Y.: Contrasting patterns of early twenty-first-century glacier mass change in the Himalayas, Nature, 488, 495-498, 10.1038/nature11324, 2012.

Kaab, A., Jacquemart, M., Gilbert, A., Leinss, S., Girod, L., Huggel, C., Falaschi, D., Ugalde, F., Petrakov, D., Chernomorets, S., Dokukin, M., Paul, F., Gascoin, S., Berthier, E., and Kargel, J. S.: Sudden large-volume detachments of low-angle mountain glaciers more frequent

550   than thought?, Cryosphere, 15, 1751-1785, 10.5194/tc-15-1751-2021, 2021.

Kaab, A., Kaufmann, V., Ladstadter, R., and Eiken, T.: Rock glacier dynamics: implications from high-resolution measurements of surface velocity fields, 8th International Conference on Permafrost, Zurich, Switzerland, Jul 21-25, WOS:000185049300089, 501-506, 2003.

Ke, L. H., Song, C. Q., Yong, B., Lei, Y. B., and Ding, X. L.: Which heterogeneous glacier melting patterns can be robustly observed from space? A multi-scale assessment in southeastern Tibetan Plateau, Remote Sensing of Environment, 242, 10.1016/j.rse.2020.111777, 2020.

The Cryosphere
Discussions

555 Kneib, M., Miles, E. S., Buri, P., Molnar, P., McCarthy, M., Fugger, S., and Pellicciotti, F.: Interannual Dynamics of Ice Cliff Populations on Debris-Covered Glaciers From Remote Sensing Observations and Stochastic Modeling, Journal of Geophysical Research-Earth Surface, 126, 10.1029/2021jf006179, 2021.

Kneib, M., Miles, E.S., Buri, P., Fugger, S., McCarthy, M., Shaw, T.E., Chuanxi, Z., Truffer, M., Westoby, M.J., Yang, W. and Pellicciotti, F.: Sub-seasonal variability of supraglacial ice cliff melt rates and associated processes from time-lapse photogrammetry, Cryosphere,
560 10.5194/tc-16-4701-2022, 2022.

Kraaijenbrink, P., Meijer, S. W., Shea, J. M., Pellicciotti, F., De Jong, S. M., and Immerzeel, W. W.: Seasonal surface velocities of a Himalayan glacier derived by automated correlation of unmanned aerial vehicle imagery, Annals of Glaciology, 57, 103-113, 10.3189/2016AoG71A072, 2016.

Li, T., Zhang, B. G., Cheng, X., Westoby, M. J., Li, Z. H., Ma, C., Hui, F. M., Shokr, M., Liu, Y., Chen, Z. Q., Zhai, M. X., and Li, X. Q.:
565 Resolving Fine-Scale Surface Features on Polar Sea Ice: A First Assessment of UAS Photogrammetry Without Ground Control, Remote Sensing, 11, 10.3390/rs11070784, 2019.

Maussion, F., Scherer, D., Molg, T., Collier, E., Curio, J., and Finkelnburg, R.: Precipitation Seasonality and Variability over the Tibetan Plateau as Resolved by the High Asia Reanalysis, Journal of Climate, 27, 1910-1927, 10.1175/jcli-d-13-00282.1, 2014.

McCarthy, M., Pritchard, H., Willis, I., and King, E.: Ground-penetrating radar measurements of debris thickness on Lirung Glacier, Nepal,
570 Journal of Glaciology, 63, 543-555, 10.1017/jog.2017.18, 2017.

McSaveney, M.J., 1975. The Sherman Glacier Rock Avalanche of 1964: its Emplacement and Subsequent Effects on the Glacier beneath it. Ph.D. Ohio State University,Columbus, OH, p. 403.

Messerli, A. and Grinsted, A.: Image georectification and feature tracking toolbox: ImGRAFT, Geoscientific Instrumentation Methods and Data Systems, 4, 23-34, 10.5194/gi-4-23-2015, 2015.

575 Mihalcea, C., Mayer, C., Diolaiuti, G., D'Agata, C., Smiraglia, C., Lambrecht, A., Vuillermoz, E., and Tartari, G.: Spatial distribution of debris thickness and melting from remote-sensing and meteorological data, at debris-covered Baltoro glacier, Karakoram, Pakistan, General Assembly of the International-Association-of-Geodesy/24th General Assembly of the International-Union-of-Geodesy-and-Geophysics, Perugia, ITALY, Jul 02-13, WOS:000257063000008, 49-+, 10.3189/172756408784700680, 2008.

Miles, E. S., Pellicciotti, F., Willis, I. C., Steiner, J. F., Buri, P., and Arnold, N. S.: Refined energy-balance modelling of a supraglacial
580 pond, Langtang Khola, Nepal, Annals of Glaciology, 57, 29-40, 10.3189/2016AoG71A421, 2016.

Miles, E. S., Steiner, J. F., Buri, P., Immerzeel, W. W., and Pellicciotti, F.: Controls on the relative melt rates of debris-covered glacier surfaces, Environmental Research Letters, 17, 10.1088/1748-9326/ac6966, 2022.

Miles, E. S., Willis, I., Buri, P., Steiner, J. F., Arnold, N. S., and Pellicciotti, F.: Surface Pond Energy Absorption Across Four Himalayan Glaciers Accounts for 1/8 of Total Catchment Ice Loss, Geophysical Research Letters, 45, 10464-10473, 10.1029/2018gl079678, 2018.

585 Miles, E., McCarthy, M., Dehecq, A., Kneib, M., Fugger, S., and Pellicciotti, F.: Health and sustainability of glaciers in High Mountain Asia, Nature Communications, 12, 10.1038/s41467-021-23073-4, 2021.

Mishra, N. B., Miles, E. S., Chaudhuri, G., Mainali, K. P., Mal, S., Singh, P. B., and Tiruwa, B.: Quantifying heterogeneous monsoonal melt on a debris-covered glacier in Nepal Himalaya using repeat uncrewed aerial system (UAS) photogrammetry, Journal of Glaciology, 68, 288-304, 10.1017/jog.2021.96, 2022.

590 Molg, N., Bolch, T., Rastner, P., Strozzi, T., and Paul, F.: A consistent glacier inventory for Karakoram and Pamir derived from Landsat data: distribution of debris cover and mapping challenges, Earth System Science Data, 10, 1807-1827, 10.5194/essd-10-1807-2018, 2018.

Nakawo, M., Yabuki, H., and Sakai, A.: Characteristics of Khumbu Glacier, Nepal Himalaya: recent change in the debris-covered area, in: Annals of Glaciology, Vol 28, edited by: Kleman, J., Annals of Glaciology-Series, 118-122, 10.3189/172756499781821788, 1999.

Neckel, N., Loibl, D., and Rankl, M.: Recent slowdown and thinning of debris-covered glaciers in south-eastern Tibet, Earth and Planetary

595   Science Letters, 464, 95-102, 10.1016/j.epsl.2017.02.008, 2017.

Nicholson, L. and Benn, D. I.: Calculating ice melt beneath a debris layer using meteorological data, Journal of Glaciology, 52, 463-470, 10.3189/172756506781828584, 2006.

Nuimura, T., Fujita, K., and Sakai, A.: Downwasting of the debris-covered area of Lirung Glacier in Langtang Valley, Nepal Himalaya, from 1974 to 2010, Quaternary International, 455, 93-101, 10.1016/j.quaint.2017.06.066, 2017.

600   Ostrem, G.: Ice Melting under a Thin Layer of Moraine, and the Existence of Ice Cores in Moraine Ridges, Geogr. Ann., 41, 228–230, 10.1080/20014422.1959.11907953, 1959.

Pellicciotti, F., Stephan, C., Miles, E., Herreid, S., Immerzeel, W. W., and Bolch, T.: Mass-balance changes of the debris-covered glaciers in the Langtang Himal, Nepal, from 1974 to 1999, Journal of Glaciology, 61, 373-386, 10.3189/2015JoG13J237, 2015.

Reid, T. D. and Brock, B. W.: An energy-balance model for debris-covered glaciers including heat conduction through the debris layer,

605   Journal of Glaciology, 56, 903-916, 10.3189/002214310794457218, 2010.

Reid, T. D. and Brock, B. W.: Assessing ice-cliff backwasting and its contribution to total ablation of debris-covered Miage glacier, Mont Blanc massif, Italy, Journal of Glaciology, 3439-3457, https://doi.org/10.3189/2014JoG13J045, 2014.

Reid, T. D., Carenzo, M., Pellicciotti, F., and Brock, B. W.: Including debris cover effects in a distributed model of glacier ablation, Journal of Geophysical Research-Atmospheres, 117, 10.1029/2012jd017795, 2012.

610   Rossini, M., Di Mauro, B., Garzonio, R., Baccolo, G., Cavallini, G., Mattavelli, M., De Amicis, M., and Colombo, R.: Rapid melting dynamics of an alpine glacier with repeated UAV photogrammetry, Geomorphology, 304, 159-172, 10.1016/j.geomorph.2017.12.039, 2018.

Rounce, D. R., Hock, R., McNabb, R. W., Millan, R., Sommer, C., Braun, M. H., Malz, P., Maussion, F., Mouginot, J., Seehaus, T. C., and Shean, D. E.: Distributed Global Debris Thickness Estimates Reveal Debris Significantly Impacts Glacier Mass Balance, Geophysical

615   Research Letters, 48, 10.1029/2020gl091311, 2021.

Rowan, A. V., Egholm, D. L., Quincey, D. J., Hubbard, B., King, O., Miles, E. S., Miles, K. E., and Hornsey, J.: The Role of Differential Ablation and Dynamic Detachment in Driving Accelerating Mass Loss From a Debris-Covered Himalayan Glacier, Journal of Geophysical Research-Earth Surface, 126, 10.1029/2020jf005761, 2021.

Sakai, A., Nakawo, M., and Fujita, K.: Distribution Characteristics and Energy Balance of Ice Cliffs on Debris-covered Glaciers, Nepal

620   Himalaya, Arctic, Antarctic, and Alpine Research, 34, 12–19, 10.1080/15230430.2002.12003463, 2002.

Sakai, A., Nakawo, M., and Fujita, K.: Melt rate of ice cliffs on the Lirung Glacier, Nepal Himalayas, 1996, Bulletin of Glacier Research, 810 16, 57–66, 1998.

Sato, Y., Fujita, K., Inoue, H., Sunako, S., Sakai, A., Tsushima, A., Podolskiy, E. A., Kayastha, R., and Kayastha, R. B.: Ice Cliff Dynamics of Debris-Covered Trakarding Glacier in the Rowaling Region, Nepal Himalaya, Frontiers in Earth Science, 9,

625   10.3389/feart.2021.623623, 2021.

Scherler, D., Wulf, H., and Gorelick, N.: Global Assessment of Supraglacial Debris-Cover Extents, Geophysical Research Letters, 45, 11798-11805, 10.1029/2018gl080158, 2018.

Shean, D. E., Bhushan, S., Montesano, P., Rounce, D. R., Arendt, A., and Osmanoglu, B.: A Systematic, Regional Assessment of High Mountain Asia Glacier Mass Balance, Frontiers in Earth Science, 7, 10.3389/feart.2019.00363, 2020.

630   Shi, Y., Liu, S., Ye, B., Liu, C. and Wang, Z.: Concise glacier inventory of China, Shanghai Popular Science Press, Shanghai, China, 2008.

Shugar, D. H. and Clague, J. J.: The sedimentology and geomorphology of rock avalanche deposits on glaciers, Sedimentology, 58, 1762-1783, 10.1111/j.1365-3091.2011.01238.x, 2011.

Steiner, J. F., Pellicciotti, F., Bur, P., Miles, E. S., Immerzeel, W. W., and Reid, T. D.: Modelling ice-cliff backwasting on a debris-covered glacier in the Nepalese Himalaya, Journal of Glaciology, 61, 889-907, 10.3189/2015JoG14J194, 2015.

635   Tadono, T., Ishida, H., Oda, F., Naito, S., Minakawa, K., and Iwamoto, H.: Precise Global DEM Generation by ALOS PRISM, ISPRS Ann. Photogramm. Remote Sens. Spatial Inf. Sci., II-4, 71–76, https://doi.org/10.5194/isprsannals-II-4-71-2014, 2014.

Van der Veen, C.J. (2013). Fundamentals of Glacier Dynamics (2nd ed.). CRC Press. https://doi.org/10.1201/b14059.

Vincent, C., Wagnon, P., Shea, J. M., Immerzeel, W. W., Kraaijenbrink, P., Shrestha, D., Soruco, A., Arnaud, Y., Brun, F., Berthier, E., and Sherpa, S. F.: Reduced melt on debris-covered glaciers: investigations from Changri Nup Glacier, Nepal, Cryosphere, 10, 1845-1858,
640   10.5194/tc-10-1845-2016, 2016.

Wang, W. C., Yao, T. D., and Yang, X. X.: Variations of glacial lakes and glaciers in the Boshula mountain range, southeast Tibet, from the 1970s to 2009, Annals of Glaciology, 52, 9-17, 10.3189/172756411797252347, 2011.

Westoby, M. J., Brasington, J., Glasser, N. F., Hambrey, M. J., and Reynolds, J. M.: 'Structure-from-Motion' photogrammetry: A low-cost, effective tool for geoscience applications, Geomorphology, 179, 300-314, 10.1016/j.geomorph.2012.08.021, 2012.

645   Westoby, M. J., Rounce, D. R., Shaw, T. E., Fyffe, C. L., Moore, P. L., Stewart, R. L., and Brock, B. W.: Geomorphological evolution of a debris-covered glacier surface, Earth Surface Processes and Landforms, 45, 3431-3448, 10.1002/esp.4973, 2020.

Xu, S. Y., Fu, P., Quincey, D., Feng, M. L., Marsh, S., and Liu, Q.: UAV-based geomorphological evolution of the Terminus Area of the Hailuogou Glacier, Southeastern Tibetan Plateau between 2017 and 2020, Geomorphology, 411, 10.1016/j.geomorph.2022.108293, 2022

Yang, W., Guo, X. F., Yao, T. D., Zhu, M. L., and Wang, Y. J.: Recent accelerating mass loss of southeast Tibetan glaciers and the
650   relationship with changes in macroscale atmospheric circulations, Climate Dynamics, 47, 805-815, 10.1007/s00382-015-2872-y, 2016.

Yang, W., Yao, T. D., Guo, X. F., Zhu, M. L., Li, S. H., and Kattel, D. B.: Mass balance of a maritime glacier on the southeast Tibetan Plateau and its climatic sensitivity, Journal of Geophysical Research-Atmospheres, 118, 9579-9594, 10.1002/jgrd.50760, 2013.

Yang, W., Yao, T. D., Zhu, M. L., and Wang, Y. J.: Comparison of the meteorology and surface energy fluxes of debris-free and debris-covered glaciers in the southeastern Tibetan Plateau, Journal of Glaciology, 63, 1090-1104, 10.1017/jog.2017.77, 2017.

655   Yang, W., Zhao, C. X., Westoby, M., Yao, T. D., Wang, Y. J., Pellicciotti, F., Zhou, J. M., He, Z., and Miles, E.: Seasonal Dynamics of a Temperate Tibetan Glacier Revealed by High-Resolution UAV Photogrammetry and In Situ Measurements, Remote Sensing, 12, 10.3390/rs12152389, 2020.

Yao, T. D., Thompson, L., Yang, W., Yu, W. S., Gao, Y., Guo, X. J., Yang, X. X., Duan, K. Q., Zhao, H. B., Xu, B. Q., Pu, J. C., Lu, A. X., Xiang, Y., Kattel, D. B., and Joswiak, D.: Different glacier status with atmospheric circulations in Tibetan Plateau and surroundings,
660   Nature Climate Change, 2, 663-667, 10.1038/nclimate1580, 2012.

Ye, D. and Gao, Y.: Meteorology of the Tibetan Plateau, Science Press, Beijing, 1979.

Zhang, Y., Fujita, K., Liu, S. Y., Liu, Q., and Nuimura, T.: Distribution of debris thickness and its effect on ice melt at Hailuogou glacier, southeastern Tibetan Plateau, using in situ surveys and ASTER imagery, Journal of Glaciology, 57, 1147-1157, 10.3189/002214311798843331, 2011.

665   Zhao, C. X., Yang, W., Westoby, M., An, B. S., Wu, G. J., Wang, W. C., Wang, Z. Y., Wang, Y. J., and Dunning, S.: Brief communication: An approximately 50 Mm³ ice-rock avalanche on 22 March 2021 in the Sedongpu valley, southeastern Tibetan Plateau, Cryosphere, 16, 1333-1340, 10.5194/tc-16-1333-2022, 2022.

Data availability

The UAV-derived orthomosaics and DEMs of this study are openly available in Zenodo at
670   https://doi.org/10.5281/zenodo.7350479. The above data will be available when this paper is final published in TC.

Author Contributions

CZ, WY, ESM, MW, MK, FP designed the study and completed the data analysis. WY supervised the study. WY, CZ, ESM, MW, MK, YW, ZH conducted the fieldwork. All authors contributed to the writing and revision of the paper.

Funding

Acknowledgements

Competing interests

685   The authors have the following competing interests: At least one of the coauthors is a member of the editorial board of The Cryosphere.